Supporting Information

NiFeLDH/$Mo_{4/3}B_{2-x}T_z$/NF composite electrodes prepared to enhance oxygen evolution performance

Lulu Xu, Peng Yang, Ruilong Ye, Xingcai Wu*, Yourong Tao*

Key Laboratory of Mesoscopic Chemistry of MOE, State Key Laboratory of Coordination Chemistry, School of Chemistry and Chemical Engineering, Nanjing University, Nanjing 210093, China.

*Correspondence:wuxingca@nju.edu.cn (X.W);yrtao@nju.edu.cn (Y. T)

Preparation of $(Mo_{2/3}Y_{1/3})_2AlB_2$

Molybdenum powder, yttrium powder, aluminum powder, and boron powder were mixed according to the ratio of 4:2:3:6 (the total amount is about 2g), and then ground in a mortar until the mixture is very uniform (the grinding time is half an hour above). The mixed metal powder was placed in a corundum container , and then placed in a tube furnace with an argon atmosphere for high-temperature calcination. , The temperature was raised to 1410℃from 30℃ in 2 hours, and kept for 8 hours, and then the temperature was naturally lowered to room temperature.

Preparation of two-dimensional material $Mo_{4/3}B_{2-x}T_z$.

1g of precursor $(Mo_{2/3}Y_{1/3})_2AlB_2$ powder was weighed, ground through a 200-mesh screen, then placed in a polytetrafluoroethylene container, added 20 ml of 50% hydrofluoric acid solution, and placed in water at 40°C with heating and stirring for 24 h. And then the mixture was transferred to a 50 ml centrifuge tube, centrifuged at 11000 rpm for 5min to remove hydrofluoric acid, then added 20 ml of anaerobic water to ultrasonically clean the lower layer of powder, then centrifuged at 11000 rpm for 5 min to remove the washing solution, repeated 3 times. In order to further stratify, 10 ml of 20% tetrabutylammonium hydroxide solution was added to the centrifuge tube with the samples, and sonicated for 5min, and then centrifuged at a speed of 11000 rpm for 5 min to remove excess tetrabutylammonium hydroxide solution, and washed off excess tetrabutylammonium hydroxide solution with ethanol, and repeated 3 times. Then it was wash off the excess ethanol with anaerobic water and repeat this step 3 times. It did not no shake the test tube to avoid stratification failure. Then we added 10ml of anaerobic water to the powder in the lower layer, and sonicate for 10 min. Then centrifuge at 2000 rpm for 10 min, and then taked the upper suspension to obtain 2 mg/ml $Mo_{4/3}B_{2-x}T_z$ 2D nanosheet suspension.

Fig. S1 analysis

Fig. S1a is the AFM image of $Mo_{4/3}B_{2-x}T_z$ suspension drop on silicon wafer. Before taking the AFM image, the bright light distribution and light color on the surface of the sample was observed with an ordinary microscope. After observation, it is found that there are more bright color areas, which can be seen to contain more two-dimensional materials. From Fig. S1a, we can see light-colored flakes at the bottom of the image. The planar size of the flakes ranges from tens of square nanometers to hundreds of square nanometers. The contrast with the light color is the color Deep silicon substrate. We use the cutting tool to cut, from one side of the silicon wafer substrate through the light-colored sample to the other side of the silicon wafer substrate, and observe the height change of the cutting surface, as shown in Fig. S1a red and green data image, the average thickness of the light-colored sample is 2.88nm, reaching the thickness dimension of ultrathin nanosheets. Fig. S1b shows the Tyndall effect of the colloid formed by mixing $Mo_{4/3}B_{2-x}T_z$ nanosheets with water under red laser irradiation. We will prepare $Mo_{4/3}B_{2-x}T_z$ nanosheet colloid and we will see the Tyndall effect by placing it under the red laser for irradiation, which can prove that the size of the sample we prepared is relatively small, reaching the nanometer level (1nm-100nm), which further shows that the microscopic scale of $Mo_{4/3}B_{2-x}T_z$ material is at the nanometer level. Fig. S1c is a scanning electron microscope (SEM) picture of the precursor

$(Mo_{2/3}Y_{1/3})_2AlB_2$. From the picture, we can see a relatively obvious layered structure, which is basically consistent with the morphology synthesized by Zhou et al. Fig. S1d is the SEM image of the $Mo_{4/3}B_{2-x}T_z$ suspension drop on the silicon wafer. From the image, we can see the obvious layered structure. Due to the special electronic structure of the ultrathin nanosheets of $Mo_{4/3}B_{2-x}T_z$, $Mo_{4/3}B_{2-x}T_z$ is relatively sensitive to electrons, a large number of which beams need to be emitted when scanning electron microscope imaging. As shown in figure, the brighter area in Fig. S1d is the result of being affected by the electron beam during imaging.

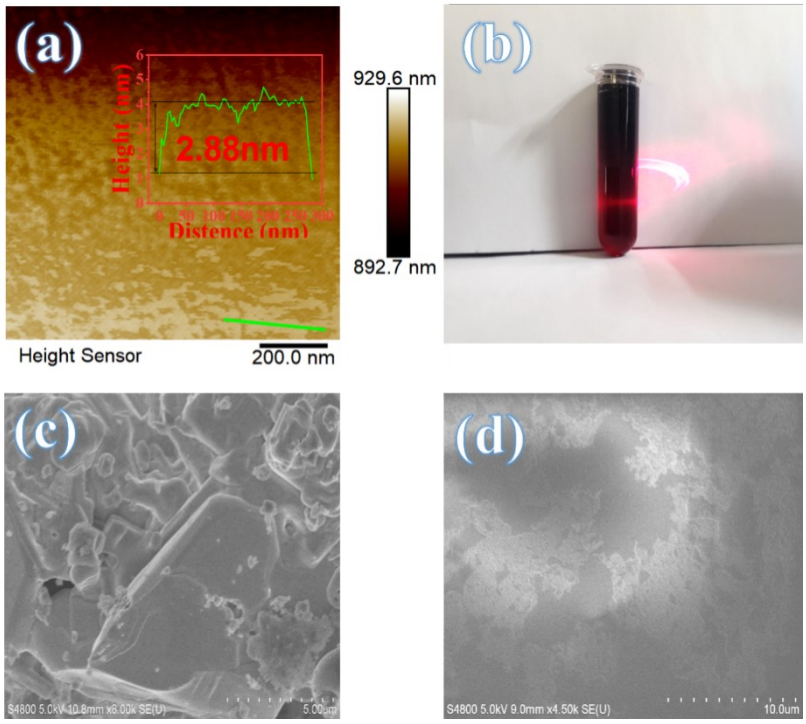

Fig. S1. (a) atomic force microscope (AFM) image of $Mo_{4/3}B_{2-x}T_z$ nanosheets on silicon wafers. (b) The Tyndall effect of the colloid formed by mixing $Mo_{4/3}B_{2-x}T_z$ nanosheets with water under red laser irradiation. (c) scanning electron microscope (SEM) image of the precursor $(Mo_{2/3}Y_{1/3})_2AlB_2$. (d) SEM image of $Mo_{4/3}B_{2-x}T_z$ nanosheets on silicon wafers.

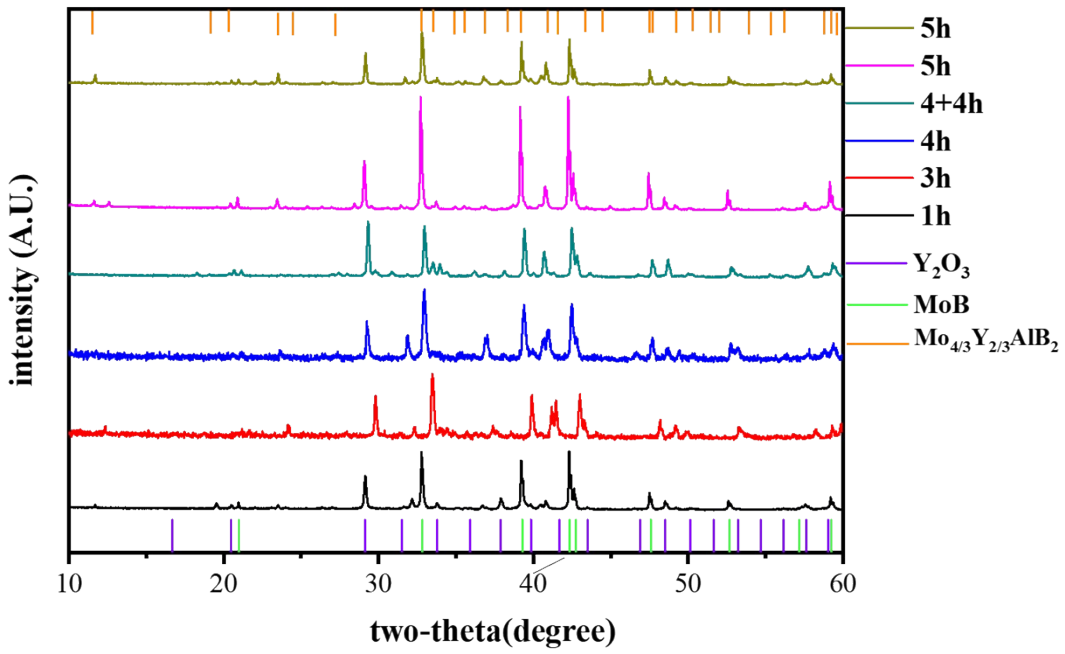

Fig. S2. XRD pattern of precursor prepared by reaction at different time

XRD analysis

Fig. S3c is the XRD image of the two-dimensional material precursor $(Mo_{2/3}Y_{1/3})_2AlB_2$. There are three sets of data in Fig. S3c, among which the red ones are $(Mo_{2/3}Y_{1/3})_2AlB_2$. $(Mo_{2/3}Y_{1/3})_2AlB_2$ has four characteristic peaks, 2θ is 12, 24 , 33 d and 40.5 degrees, and the main peak of 33 degrees is the common peak of $(Mo_{2/3}Y_{1/3})_2AlB_2$ and MoB, which is consistent with the original XRD in the literature. The synthesis process of the precursor $(Mo_{2/3}Y_{1/3})_2AlB_2$ is a high temperature solid-state reaction. The Mo, Y, Al, and B elemental powders are ground and mixed for a high temperature reaction, which will produce some miscellaneous items. The main miscellaneous items are molybdenum boride and yttrium oxide. The green

data and blue data in Fig. S3c represent the standard PDF card data of yttrium oxide and molybdenum boride. After comparing with the synthetic sample, it is found that the sample does contain miscellaneous yttrium oxide and molybdenum boride, but the main composition is $(Mo_{2/3}Y_{1/3})_2AlB_2$. $(Mo_{2/3}Y_{1/3})_2AlB_2$ is placed in 50% HF aqueous solution acid for acetolysis to remove the middle layer Al layer and Y layer, so as to obtain a two-dimensional material. The sample after acid hydrolysis was separated and dried in vacuum for XRD test. The data plot in black in Fig. S3a is the sample after acid hydrolysis. After comparison, it is found that the four main peaks of $(Mo_{2/3}Y_{1/3})_2AlB_2$ have all decreased. It can be seen that $(Mo_{2/3}Y_{1/3})_2AlB_2$ has been successfully etched away. At 10 degrees of 2 theta, it can be seen that a strong peak appears in the black data line, which is a diffraction peak at the distance between different layers of the two-dimensional material $Mo_{4/3}B_{2-x}T_z$. Fig. S3b is the comparison pattern of XRD of $(Mo_{2/3}Y_{1/3})_2AlB_2$ and $(Mo_{2/3}Y_{1/3})_2AlB_2$ etched in 40% HF aqueous solution at 40 °C for 24 hours under stirring conditions. Among them, the black data map is the XRD image of the sample obtained after etching. Observing the black data map, it can be found that the four characteristic peaks of $(Mo_{2/3}Y_{1/3})_2AlB_2$ have slightly decreased. It is worth noting that the main peak of 40.5 degrees of 2 theta has been significantly reduced and a new peak appears at about 10 degrees of 2 theta after 40% HF etching. This is also the diffraction peak that occurs at the distance

between different layers of the two-dimensional material $Mo_{4/3}B_{2-x}T_z$, but This peak is much smaller than that in Fig. S3a. It can be seen that 40% hydrofluoric acid can also etch the precursor $(Mo_{2/3}Y_{1/3})_2AlB_2$ to obtain the two-dimensional material $Mo_{4/3}B_{2-x}T_z$, but the etching degree is small, so the XRD contrast difference before and after etching not very noticeable.

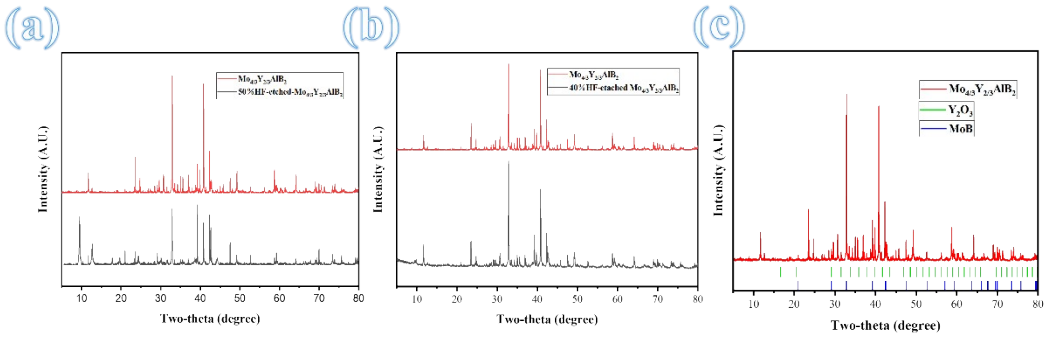

Fig. S3. (a) XRD comparison image of the precursor $(Mo_{2/3}Y_{1/3})_2AlB_2$ before etching and after 50% HF etching for 24 hours. (b) XRD comparison image of the precursor $(Mo_{2/3}Y_{1/3})_2AlB_2$ before etching and after 40% HF etching for 24 hours.
(c) XRD image of the precursor $(Mo_{2/3}Y_{1/3})_2AlB_2$.

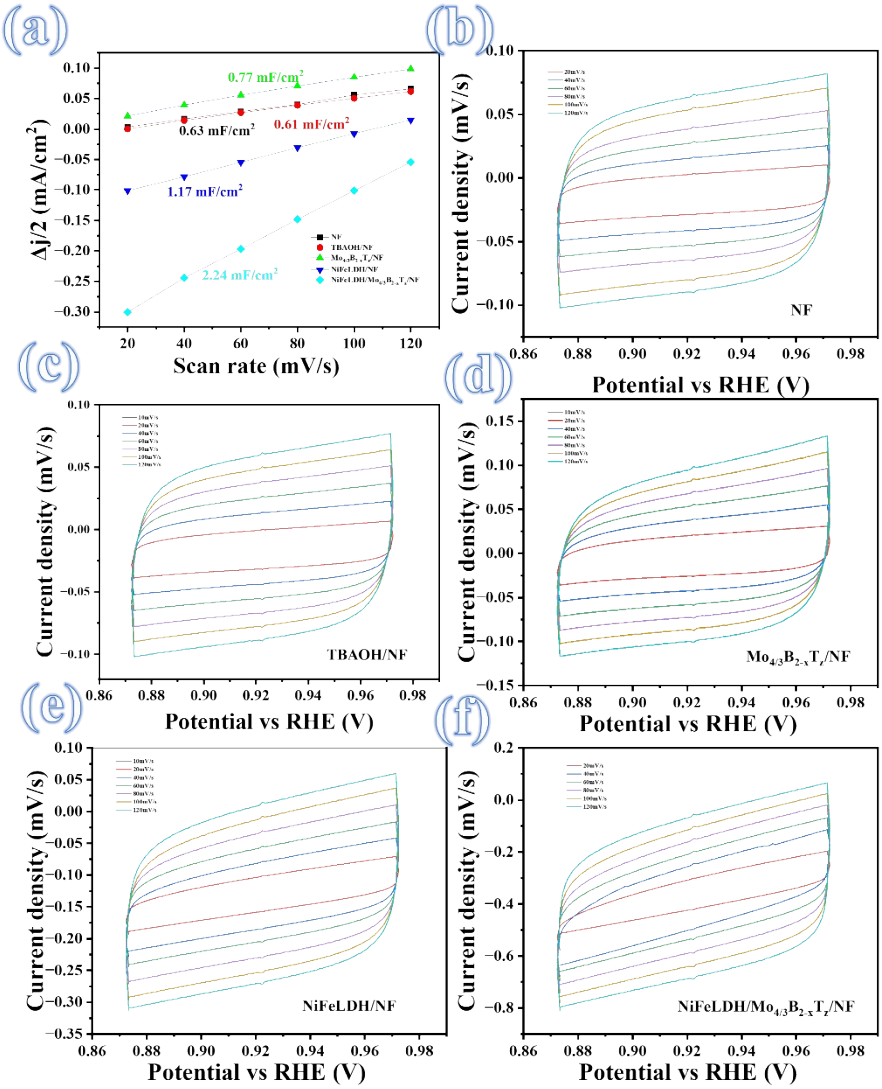

Fig. S4. (a) the pattern of C_{dl} of NF, TBAOH/NF, $Mo_{4/3}B_{2-x}T_z$/NF, NiFeLDH/NF, NiFeLDH/$Mo_{4/3}B_{2-x}T_z$/NF. (b) Curves of CV of NF. (c) Curves of CV of TBAOH/NF. (d) Curves of CV of $Mo_{4/3}B_{2-x}T_z$/NF. (e) Curves of CV of NiFeLDH/NF. (e) Curves of CV of NiFeLDH/ $Mo_{4/3}B_{2-x}T_z$/NF.

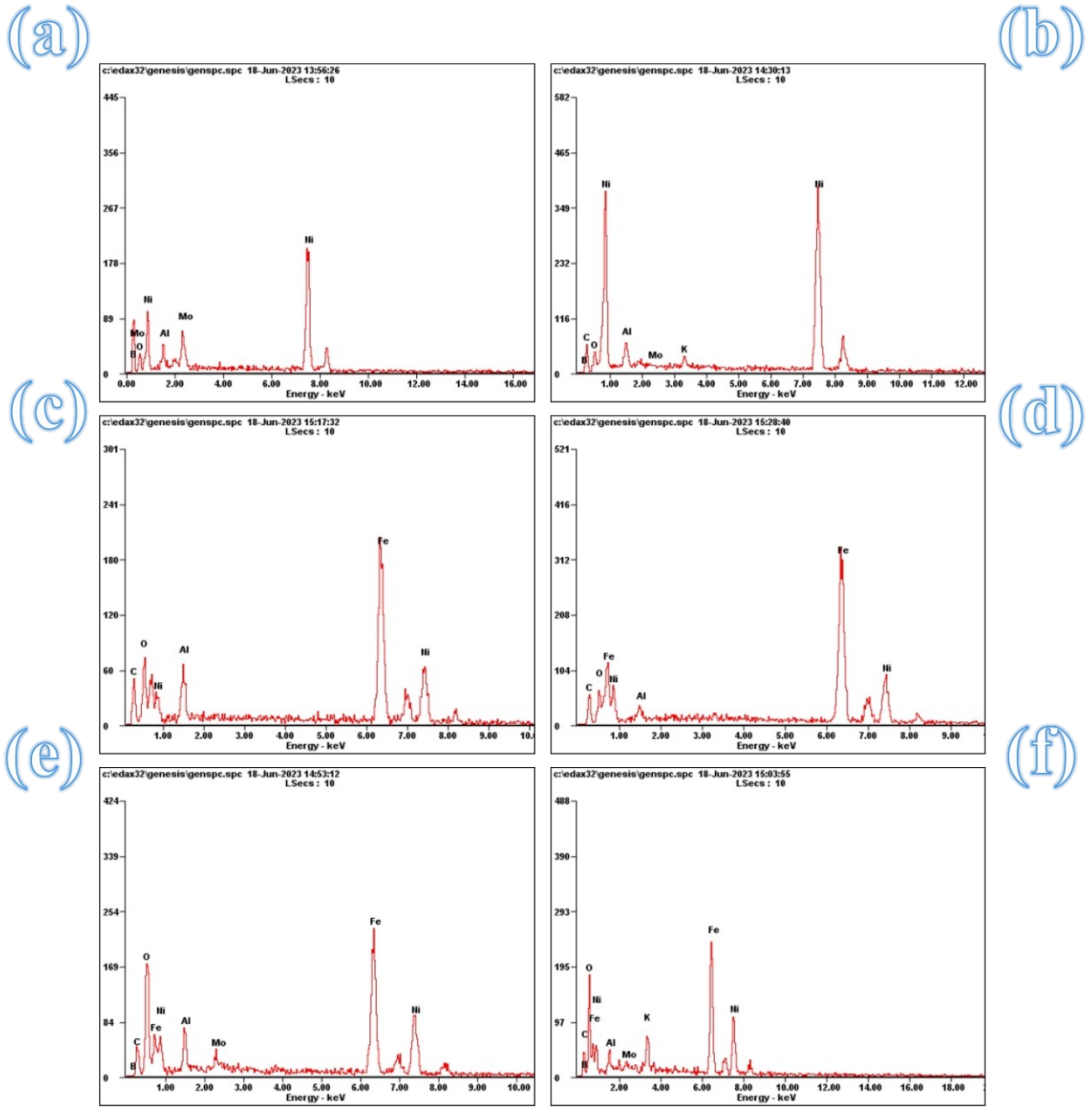

Element	Wt %	At %
B K	17.01	37.51
O K	24.85	37.03
F K	00.40	00.50
NiL	20.86	08.47
AlK	02.78	02.46
MoL	02.80	00.69
FeK	30.05	12.83

Fig. S5. (a) the pattern of EDX of $Mo_{4/3}B_{2-x}T_z$/NF before electrochemical test. (b) the pattern of EDX of $Mo_{4/3}B_{2-x}T_z$ /NF after electrochemical test. (c) the pattern of EDX of NiFeLDH/NF before electrochemical test. (d) the pattern of EDX of NiFeLDH/NF after electrochemical test. (e) the pattern of EDX of NiFeLDH/ $Mo_{4/3}B_{2-x}T_z$ /NF before electrochemical test. (f) the pattern of EDX of NiFeLDH/ $Mo_{4/3}B_{2-x}T_z$/NF after electrochemical test. The bottom table is the composition of NiFeLDH/ $Mo_{4/3}B_{2-x}T_z$ /NF.

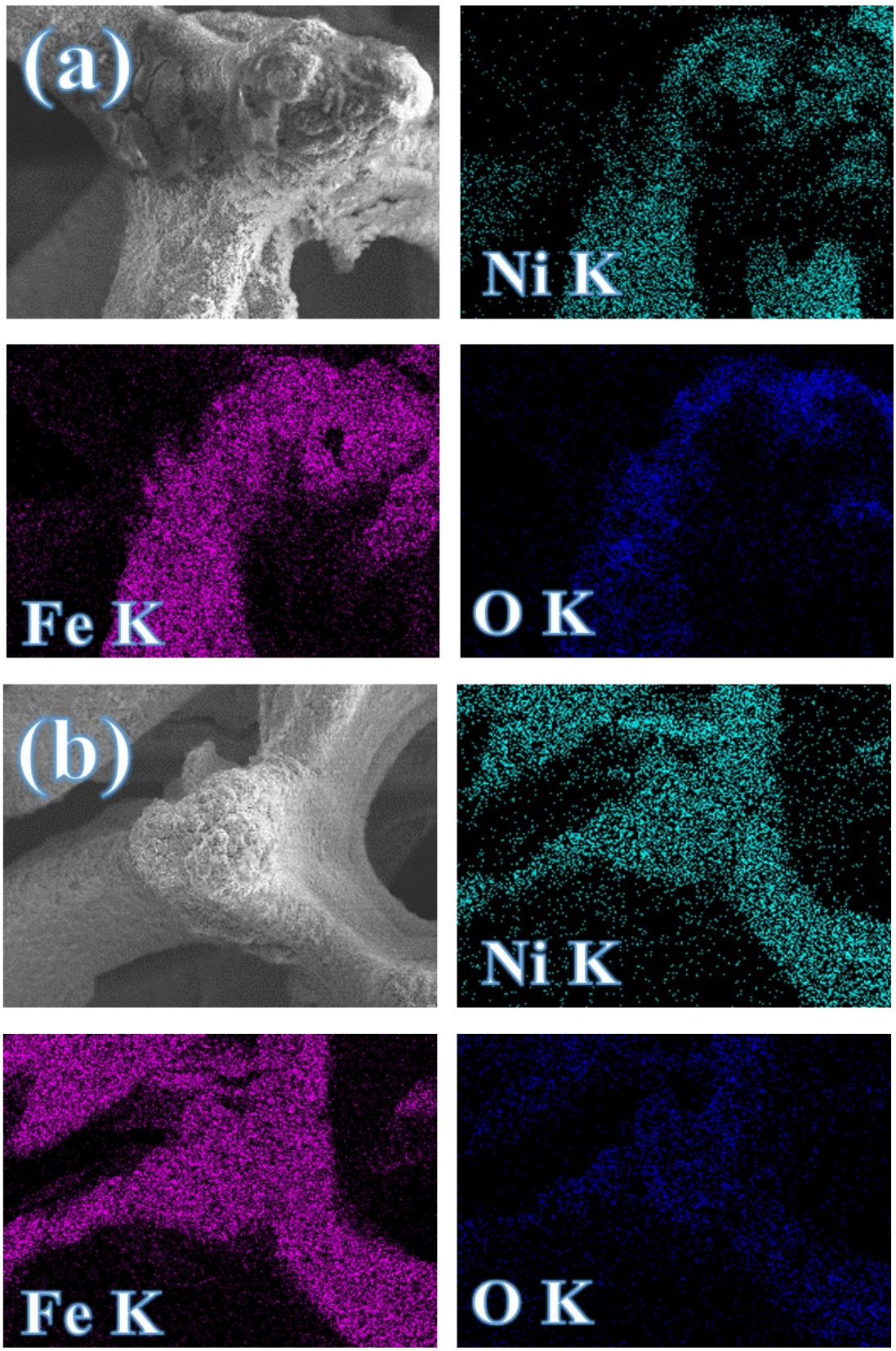

Fig. S6. (a) the Mapping images of elements of Ni,Fe,O of NiFeLDH/NF before electrochemical test. (b) the Mapping images of elements of Ni,Fe,O of NiFeLDH/NF after electrochemical test.

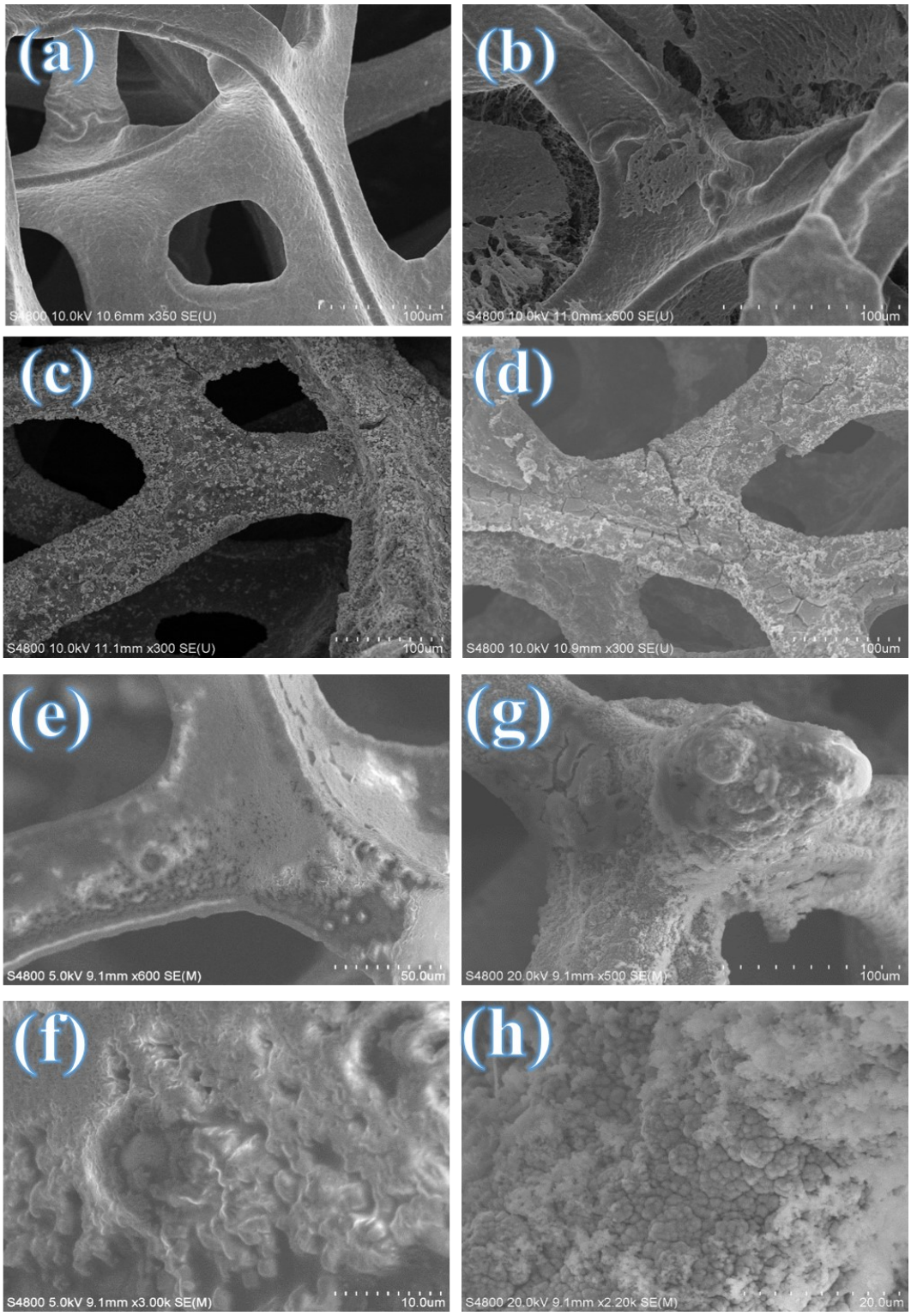

Fig. S7. (a-d) large versions of Fig. 3(a-d). (e) SEM image of $Mo_{4/3}B_{2-x}T_z$/NF. (f) large versions of (e). (g) SEM image of NiFeLDH/NF. (h) large versions of (g).

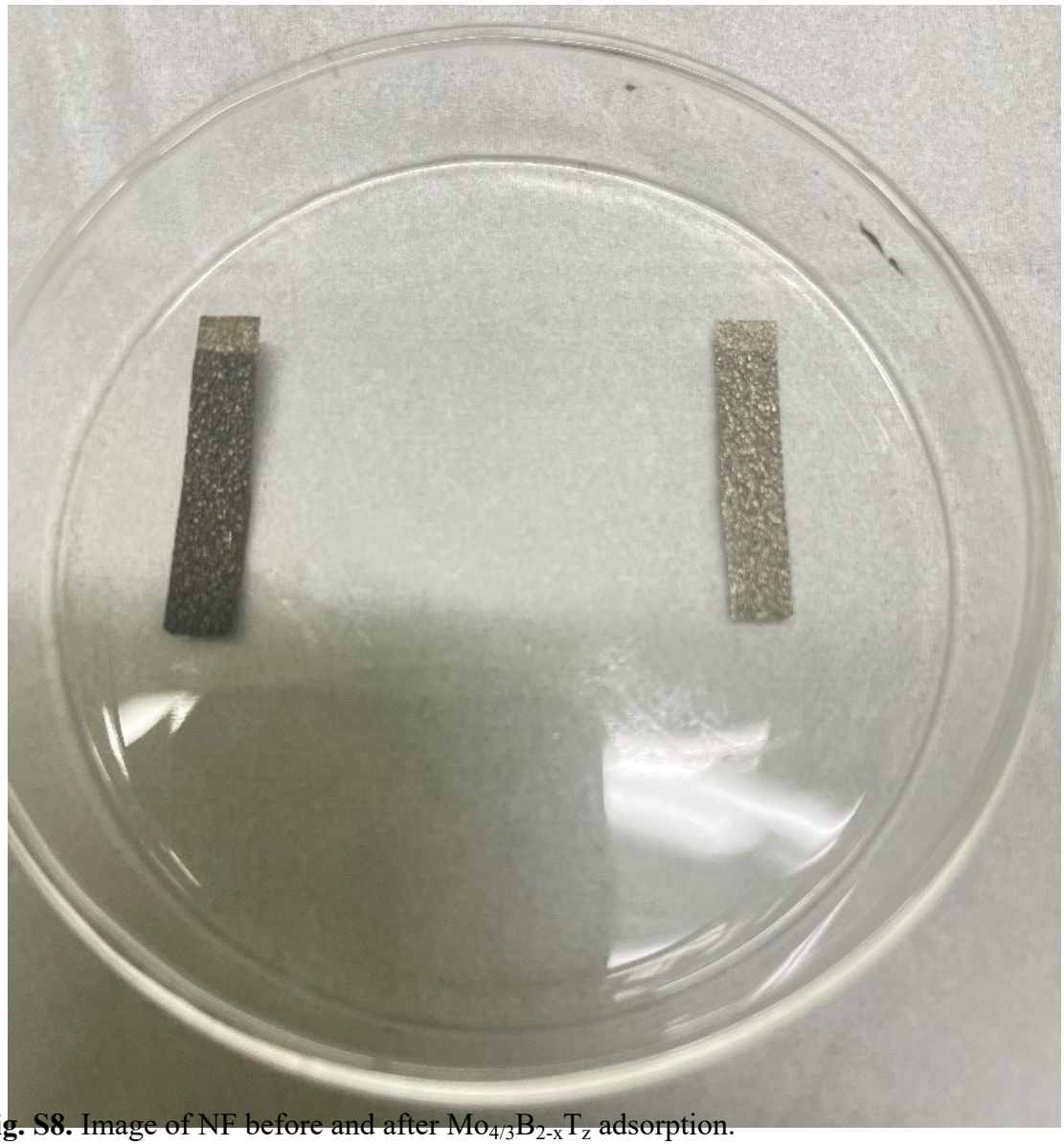

Fig. S8. Image of NF before and after $Mo_{4/3}B_{2-x}T_z$ adsorption.

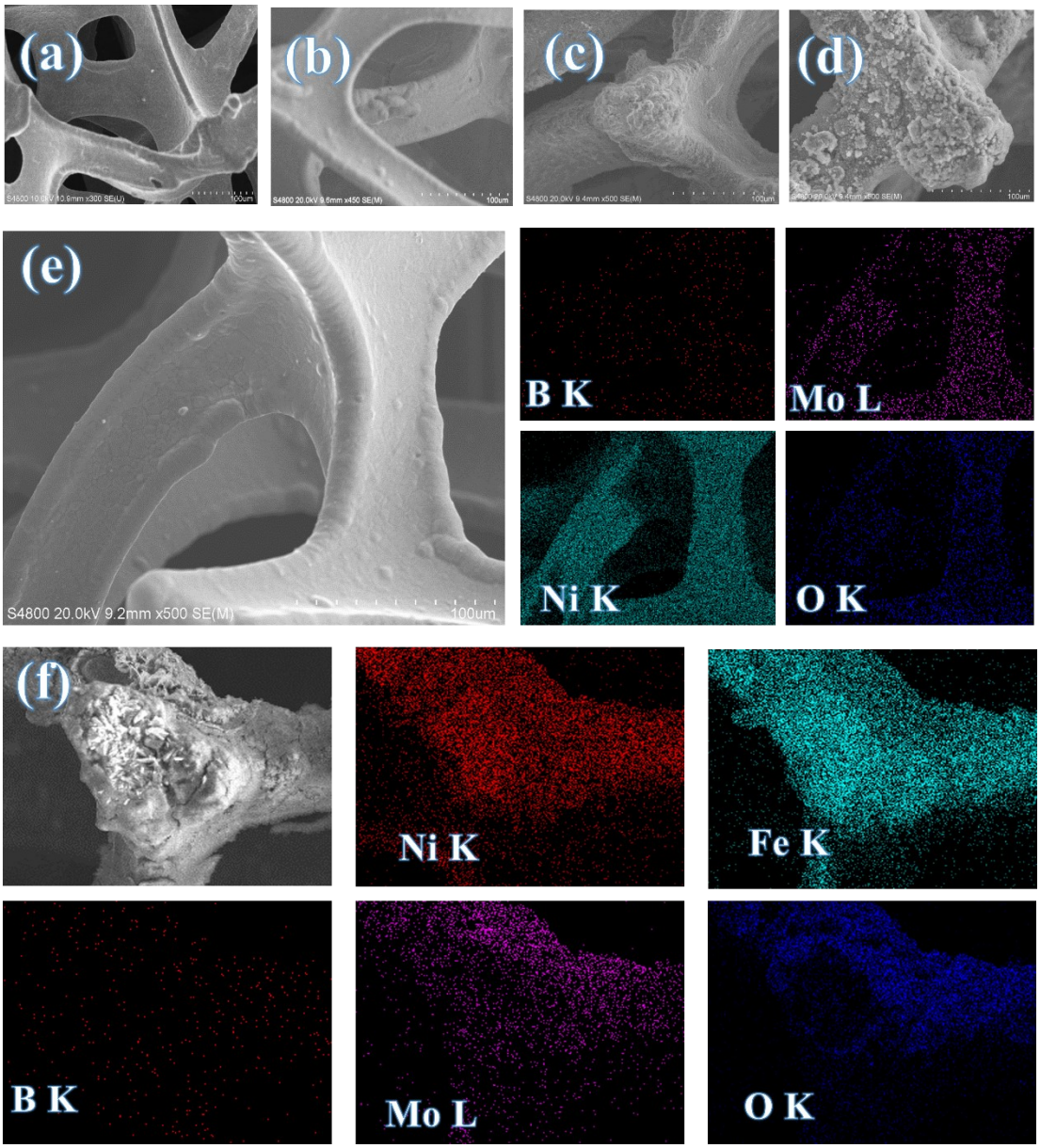

Fig. S9. (a-d) SEM images of Ni, $Mo_{4/3}B_{2-x}T_z$/NF, NiFeLDH/NF, NiFeLDH/$Mo_{4/3}B_{2-x}T_z$/NF after electrochemical testing. (e) Mapping images of elements of B, Mo, Ni, O of $Mo_{4/3}B_{2-x}T_z$/NF after electrochemical test. (f) Mapping images of elements of B, Mo, Ni, Fe and O of NiFeLDH/$Mo_{4/3}B_{2-x}T_z$/NF after electrochemical test.

Table S1. Recent progress in the research of nickel-iron oxygen evolution catalysts.

Samples	Rs (Ω)	CPE-T	CPE-P	Rp (Ω)
1M	1.069	0.012407	0.83575	6039
TBAOH/NF	1.144	0.012693	0.83229	285.7

Catalyst	**Electrolyte**	**E vs. RHE (mV) 100 mA cm^{-2}**	**Tafel slope (mV dec^{-1})**	**References**
NiFeLDH/$Mo_{4/3}B_{2-x}T_z$/NF	1 M KOH	255	45	This work
$Mo_{4/3}B_{2-x}T_z$/NF	1 M KOH	386	49	This work
Cu_3P@NiFe-LDH/CF	1 M KOH	300	39	[1]
NiFeCr-LDH	1 M KOH	250	30	[2]
$NiFe(OH)_x/Fe_{0.2}Co$-Se	1 M KOH	277	37	[3]
NiFeLDH/$Ti_3C_2T_x$/NF	1 M KOH	263	64	[4]
Ni-Ni_2P@NiFe LDH	1 M KOH	300	48	[5]
Cu_2S@NiFeLDHs/Cu	1 M KOH	286	57	[6]
Ni_3S_2-Ni_xP_y/NF@NiFe LDH	1 M KOH	298	41	[7]
NiFeLDH/Ni-S/NF	1 M KOH	258	49	[8]
NiFeLDH/$Co_{1-x}S$	1 M KOH	310	42	[9]
FNM/Co_2P-0.4	1 M KOH	300	74	[10]
$NiFe(OH)_x$/CP	1 M KOH	303	34	[11]
NiFeLDH/Cu/CF	1 M KOH	300	50	[12]

$Mo_{4/3}B_{2-x}T_z$/NF	1.107	0.014905	0.87004	107.1
NiFeLDH/NF	1.100	0.385910	0.84047	1.817
NiFeLDH/$Mo_{4/3}B_{2-x}T_z$/NF	1.109	0.688600	0.82035	1.425

Table S2. The results of Nyquist plots of the samples fitted in high frequency area.

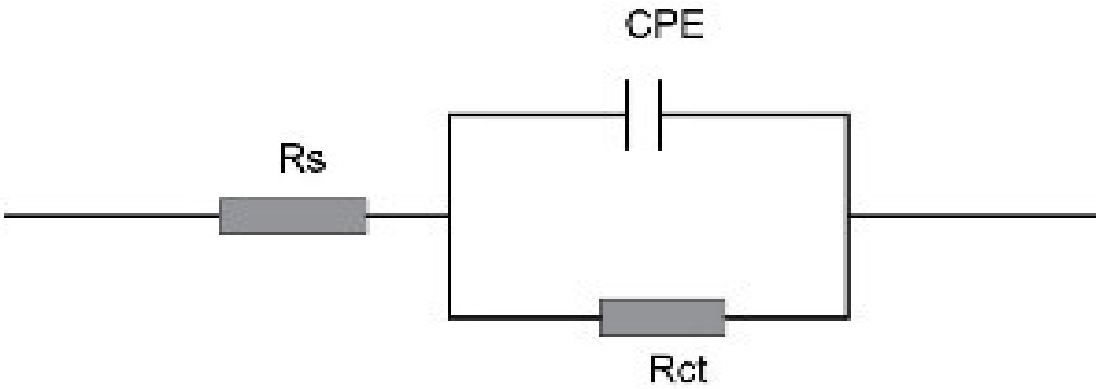

Fig. S10. The equivalent circuit of Nyquist plots of the samples fitted in high frequency area.

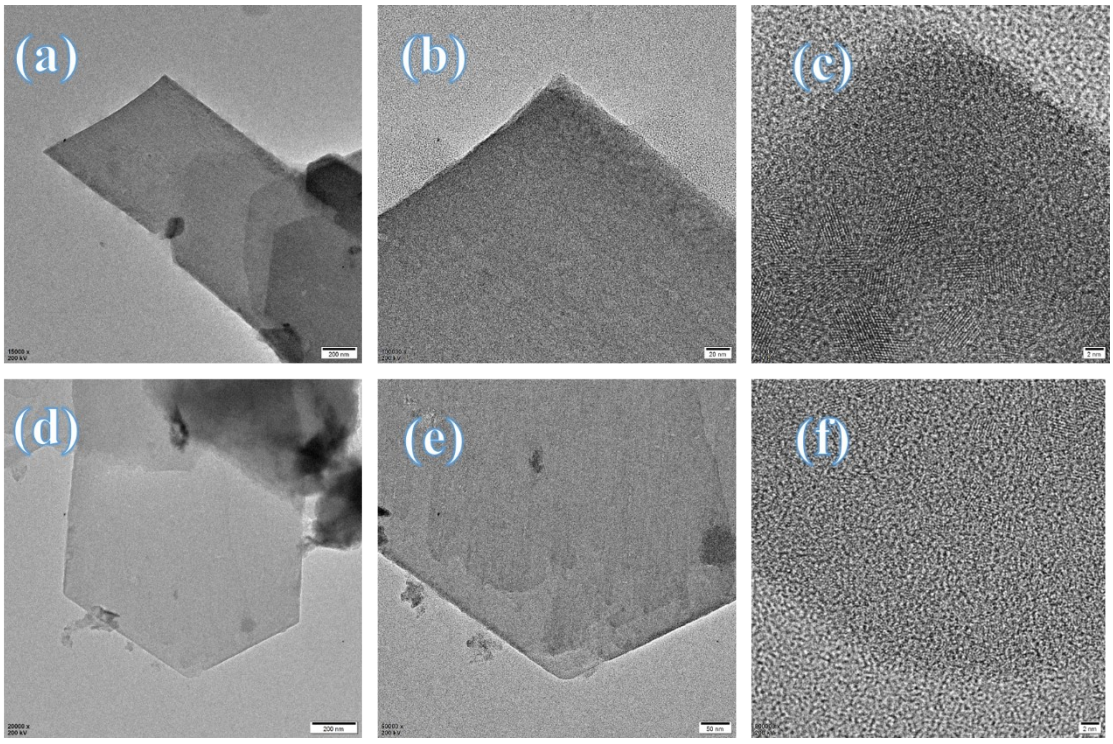

Fig. S11. (a-c) Successively enlarged TEM images of $Mo_{4/3}B_{2-x}T_z$. (d-f) Second set of Successively enlarged TEM images of $Mo_{4/3}B_{2-x}T_z$.

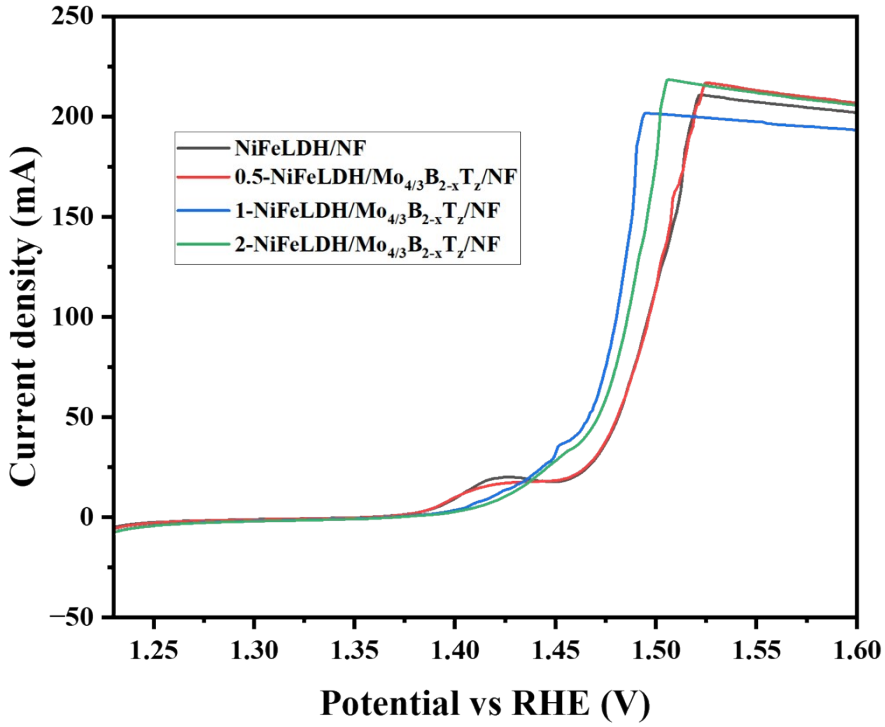

Fig. S12. The LSV curve of NiFeLDH/$Mo_{4/3}B_{2-x}T_z$/NF was prepared by adsorption of 0.5, 1 and 2 times concentration of $Mo_{4/3}B_{2-x}T_z$.

Detail DFT calculations

The spin polarization DFT calculations were carried out by the Dmol^3 module in Materials Studio 8.0 package and generalized gradient approximation with Perdew–Becke–Ernzerhof (PBE) was used for the exchange–correlation functional. The double numerical plus polarization (DNP) basis set were adopted, while an accurate DFT semi-core pseudopots (DSPP) was employed for the metal atoms. The Brillouin zone was sampled with 2×2×1 Monkhorst-Pack k-meshes for the geometry optimization, and custom TS was used for DFT-D parameters. All of the models are calculated in periodically boxes with a vacuum slab of 15 Å to separate the interaction between periodic images. The optimized bulk structures were used to construct surface slab models. A (3 × 3) MoB_2 (001) slab model of 5 layers with supercell of 9.044408× 9.044408 ×20.354049 Å ($\alpha=\beta=90^o$, $\gamma= 120^o$) was used for pure MoB_2, and c/2 $Ni(OH)_2$ crystal cell was placed on the surface of above supercell and Ni^{2+} was partly substituted for Fe^{3+} to form $Ni_2Fe_{2-x}(OH)_2/MoB_2$ (001) supercell. All the transition state configurations were confirmed through the frequency analysis. The energy, gradient and displacement convergence criteria were set as 1×10^{-5} Ha, 2×10^{-3} Å and 5×10^{-3}Å, respectively. The Gibbs free energy of each elementary step was calculated as

$$\Delta G = \Delta E+\Delta ZPE -T\Delta S$$

where ΔE is the reaction energy calculated using the spin polarization DFT method. ΔZPE and ΔS are the changes in zero-point energies and entropy during the reaction, respectively.

Whereas the OER is the four-electron process with an overall reaction ($2H_2O \rightarrow O_2 + 4H^+ + 4e^-$). The four elementary steps of OER in alkaline media are described by:

$$4OH^- + * \rightarrow *OH + 3OH^- + e^-$$

$$*OH + 3OH^- + e^- \rightarrow *O + H_2O + 2OH^- + 2e^-$$

$$*O + H_2O + 2OH^- + 2e^- \rightarrow *OOH + H_2O + OH^- + 3e^-$$

$$*OOH + H_2O + OH^- + 3e^- \rightarrow *O_2 + 2H_2O + 4e^-$$

$$*O_2 + 2H_2O + 4e^- \rightarrow O_2 + 2H_2O + 4e^- + *$$

Where * denotes an active site and OH*, O*, OOH*, and $*O_2$ represent the adsorbed intermediate at the active site. Energies every step were calculated as follows:

$$\Delta G = \Delta E + \Delta ZPE - T\Delta S + \Delta G_U + \Delta G_{pH}$$

All Gibbs free energy analysis was performed under standard conditions (U=0, pH = 0 and pH=1, 298.15 K, 1 atm).

The supercell structures were used for calculation as following: (Pink: B, Pale Green: Mo, Blue: Ni, Bluish violet: Fe, Red: O, white: H.)

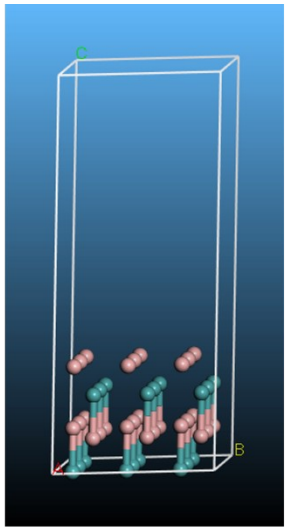

B_2Mo-001-33

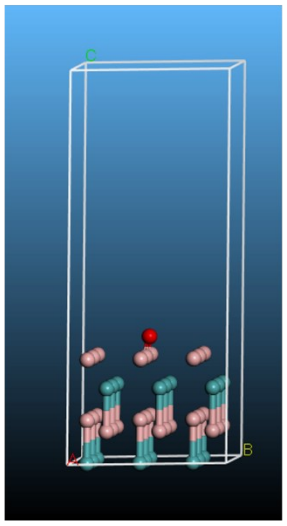

B_2Mo-001-33O

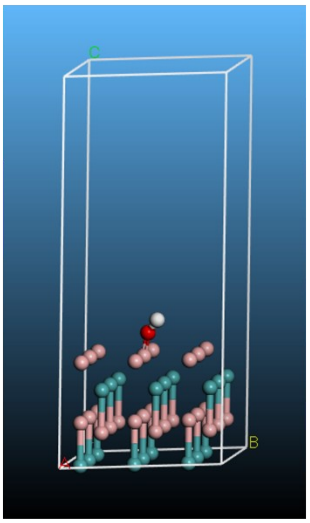

B_2Mo-001-33OH

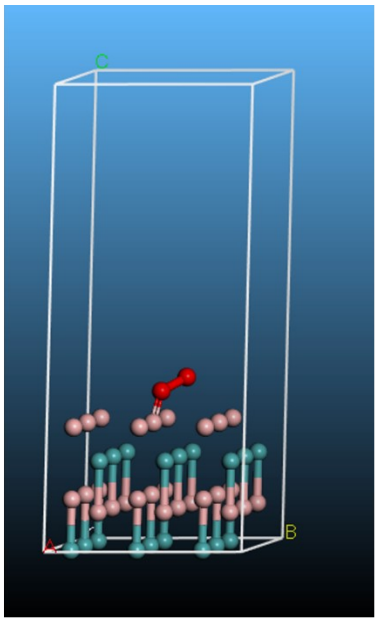

B_2Mo-001-33OO

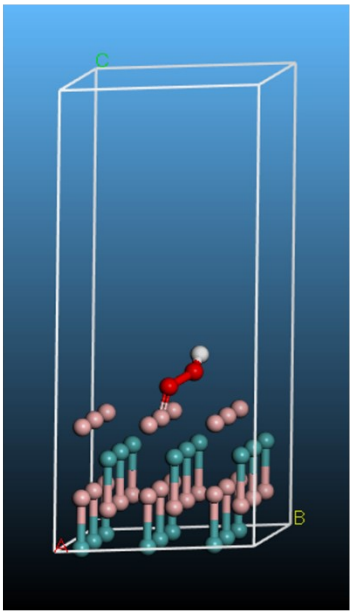

B_2Mo-001-33OOH

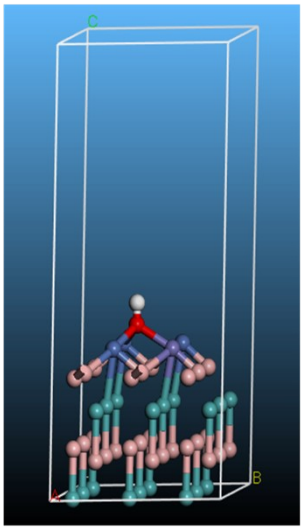

B_2Mo-001-33NIFe2a

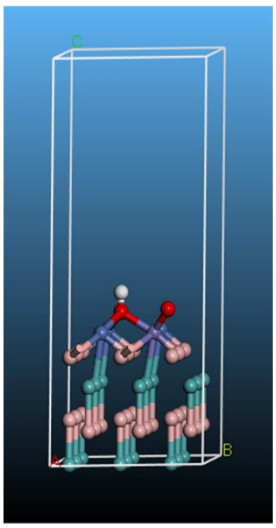

B_2Mo-001-33NIFe2aO

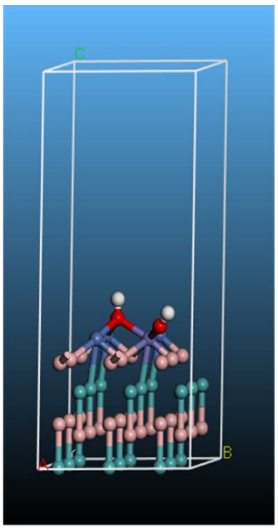

B_2Mo-001-33NIFe2aOH

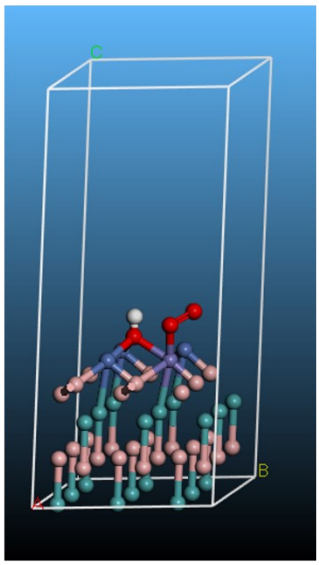

B_2Mo-001-33NIFe2aOO

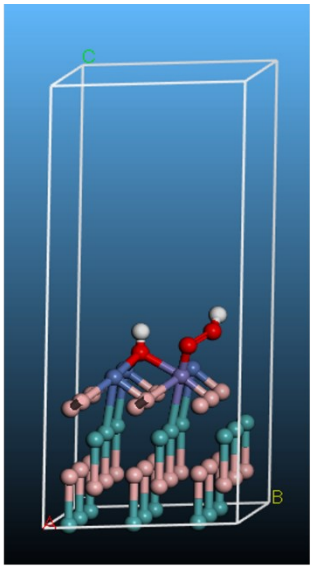

B_2Mo-001-33NIFe2aOOH

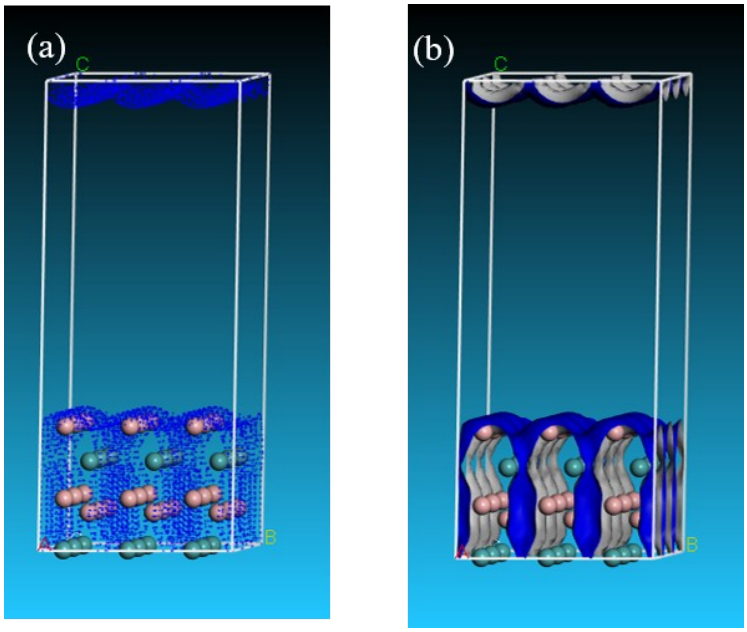

Fig. S13. Electronic density scheme of B_2Mo-001-33 (3×3 supercell of $MoB_2(001)$). (a) dot, (b) solid. (Pink: B, Pale Green: Mo, Blue: Ni, Bluish violet: Fe, Red: O, white: H.)

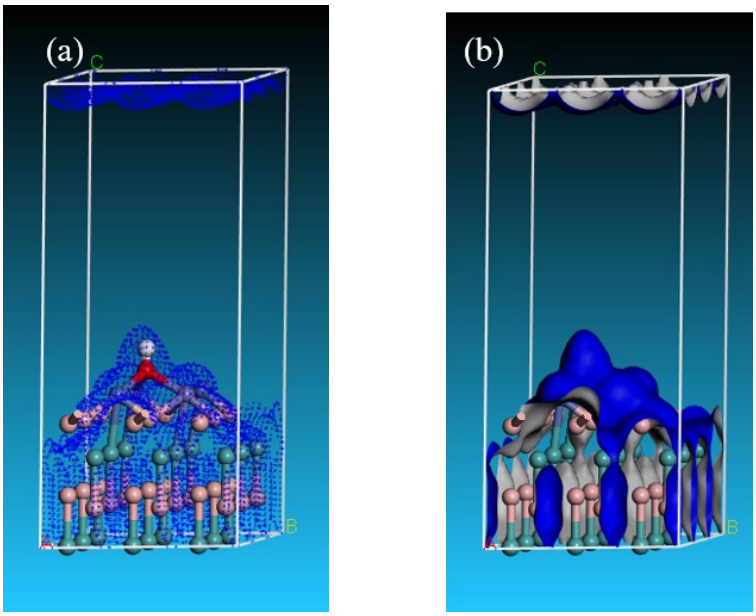

Fig. S14. Electronic density scheme of B_2Mo-001-33NIFe2a (3×3 supercell of $1/2Ni_{2-x}Fe_x(OH)_2(001)$/ $MoB_2(001)$). (a) dot, (b) solid.

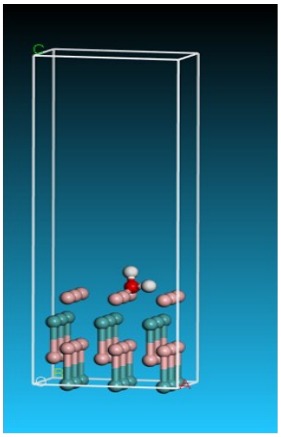

(a) B_2Mo-001-33H2OB

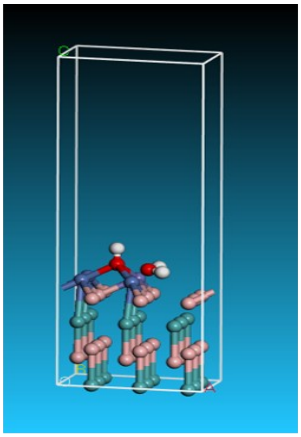

(b) B_2Mo-001-33NIFe2aH2O

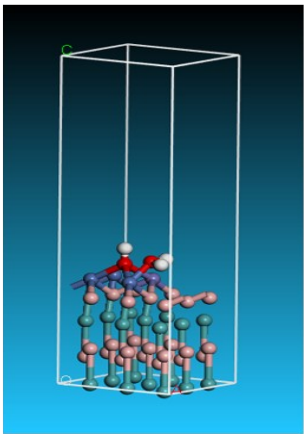

(c) B_2Mo-001-33NIFe2aH2ONi

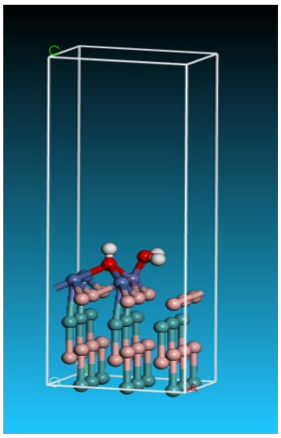

(d) B_2Mo-001-33NIFe2aH2OFe

Fig. S15. Structure Models when H_2O adsorption energy was calculated: (a) H_2O adsorbed on Boron site of 3x3 supercell of MoB_2(001); (b) H_2O adsorbed on interface site of 3×3 supercell of 1/2$Ni_{2-x}Fe_x(OH)_2$ (001)/ MoB_2(001); (c) H_2O adsorbed on Ni site of 3×3 supercell of 1/2$Ni_{2-x}Fe_x(OH)_2$ (001)/ MoB_2(001), (d) H_2O adsorbed on Fe site of 3×3 supercell of 1/2$Ni_{2-x}Fe_x(OH)_2$ (001)/ MoB_2(001); Their adsorption energies are -4.69,-2.71,-1.60, and -1.51 eV, respectively. Here E_{ads}= $E_{slab-H2O}$-(E_{slab}+E_{H2O}), where E_{ads} is water surface adsorption energy, $E_{slab-H2O}$ is energy after catalyst slab adsorbing water, and E_{slab} and E_{H2O} are energies of catalyst slab and H_2O, respectively. (Pink: B, Pale Green: Mo, Blue: Ni, Bluish violet: Fe, Red: O, white: H.)

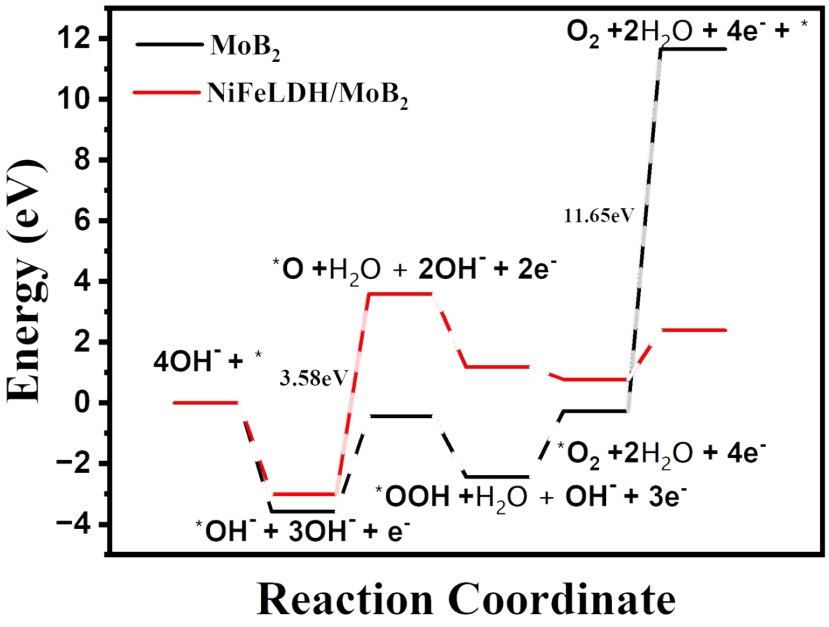

Fig. S16. Gibbs free-energy diagrams of OER (take pH into account).Pink: B, Pale Green: Mo, Blue: Ni, Bluish violet: Fe, Red: O, white: H.

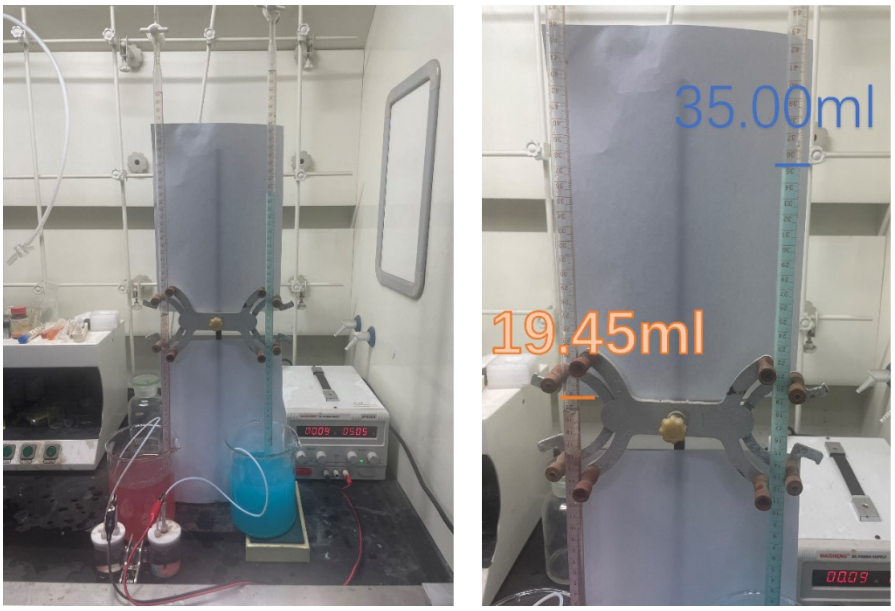

Fig. S17. Faraday efficiency experiment.

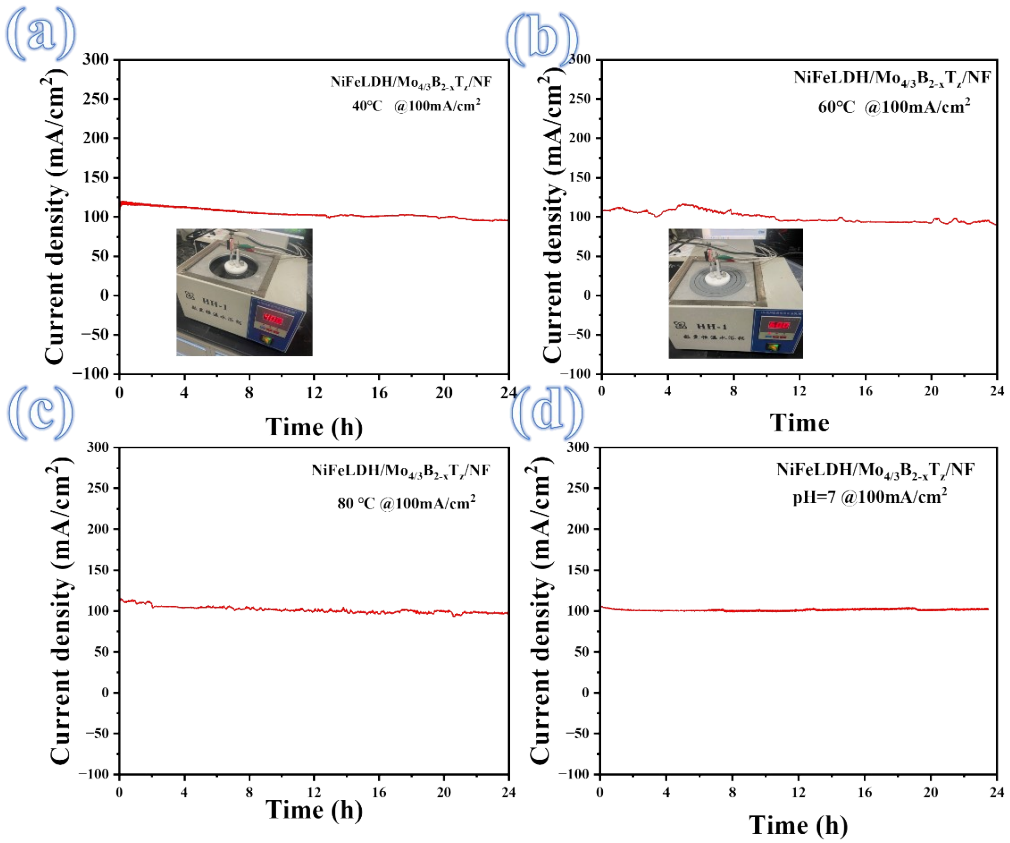

Fig. S18. (a) Stability curve at 40 ℃ in 1 M KOH. (b) Stability curve at 60 ℃ in 1 M KOH. (c) Stability curve at 80 ℃ in 1 M KOH. (d) Stability curve at room temperature and pH=7.

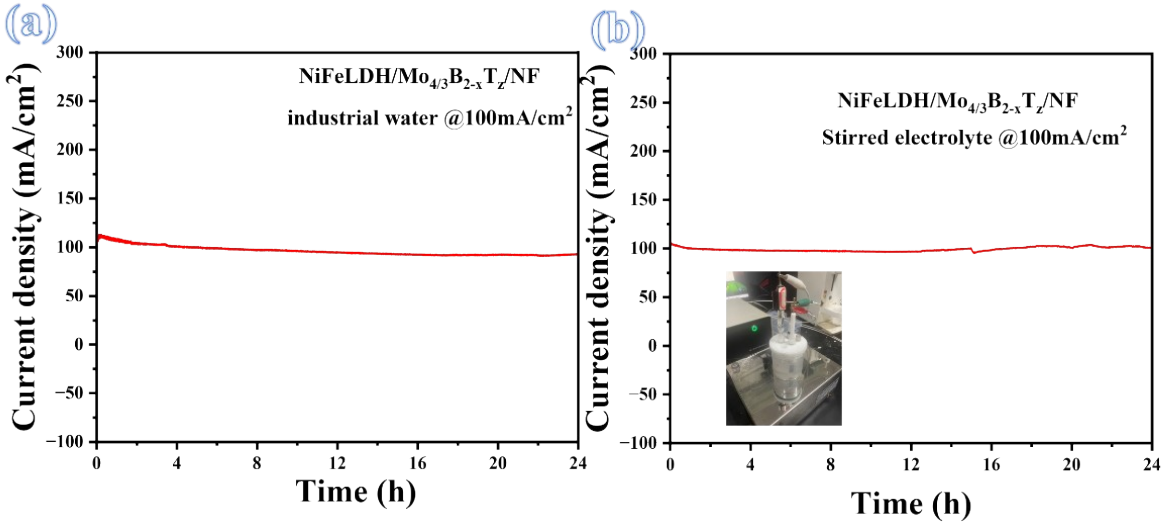

Fig. S19. (a) Stability curve in simulated industrial water source in 1 M KOH. (b) Stability curve in 1 M KOH at stirred state.

Cost analysis of preparation of NiFeLDH/$Mo_{4/3}B_{2-x}$/NF

We performed a preliminary cost analysis using the laboratory preparation process. We analyzed reagents, consumables and electric energy costs, excluding depreciation of equipment, labor costs and laboratory rental from three stages: synthesis of $(Mo_{2/3}Y_{1/3})_2AlB_2$, preparation of $Mo_{4/3}B_{2-x}T_z$ and electroplating respectively. After accounting, we found that the total cost of completing an experiment was 120.46 CNY, of which reagent 54.72 CNY (45%), consumables 47.50 CNY (40%), and electric energy cost 18.24 CNY (15%). The specific data are shown in **Table. S3.** Two 0.5 ×2 cm NiFeLDH/$Mo_{4/3}B_{2-x}T_z$/NF composite electrodes can be prepared for 120.46 CNY, which we can calculate that the cost per unit area is 30.12CNY (3.30GBP, 3.86EUR, 4.18USD). The unit area cost of platinum electrode is 60 CNY (6.59GBP, 7.69EUR, 8.34USD), So our cost is much lower than platinum electrodes. In the future, industrial production will further reduce its production costs due to scale effect.

Table S3. Cost detail of preparation of NiFeLDH/$Mo_{4/3}B_{2-x}T_z$/NF.

Stage	Cost Types	Cost items	Unit price	Dosage	Price
$(Mo_{2/3}Y_{1/3})_2AlB_2$	Reagent	Mo 2.5N	171CNY/100 g	1.085g	1.86CNY
		Y 3N	192CNY/25g	0.503g	3.86CNY
		Al 3.5N	411CNY/100g	0.229g	0.94CNY
		B 4N	101CNY/1g	0.183g	18.48CNY
	Consumable	Crucible	2CNY/one	one	2CNY
		Silicon carbide rod	80CNY/four	rods in series can be used 4 times	20CNY
		Corundum tube	300CNY /one	Corundum tube can be used 20 times	15CNY
		Argon	100CNY /40L	4L	10CNY
	Electric energy	Tubular furnace 4kW	0.5CNY/1kW·h	36kW·h	18CNY
$Mo_{4/3}B_{2-x}T_z$	Reagent	TBAOH 40wt	348CNY/250ml	15ml	20.88CNY
		Ethyl alcohol	51CNY/2.5L	25ml	0.51CNY
		HF 50%	28CNY/100ml	20ml	5.60CNY
	Consumable	Centrifuge tube	0.5CNY/one	one	0.50CNY
	Electric energy	Centrifuge 0.75kW	0.5CNY/1kW·h	0.44kW·h	0.22CNY
Electroplate	Reagent	$NiNO_3·6H_2O$	135CNY/500g	2.91g	0.8CNY
		$FeSO_4·7H_2O$	311CNY/500g	2.78g	1.7CNY
		Foamed nickel	28CNY/600cm^2	2cm^2	0.09CNY
	Electric energy	Ultrasonic machine 0.12kW	0.5CNY/1kW·h	0.02kW·h	0.01CNY
		Constant voltage power supply 0.15kW	0.5CNY/1kW·h	0.025kW·h	0.01CNY
Reagent	54.72 CNY	Consumable	47.50CNY	Electric energy	18.24CNY
total	**120.46 CNY**				
total	**13.20GBP / 15.42EUR / 16.73USD**				

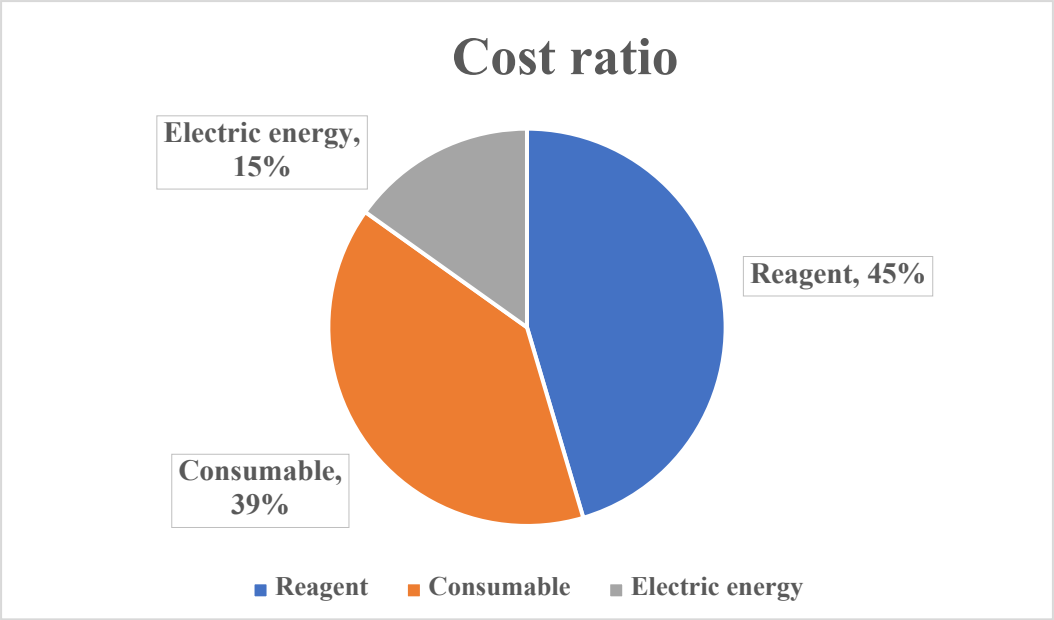

Fig. S20. Cost composition ratio of preparation of NiFeLDH/$Mo_{4/3}B_{2-x}T_z$/NF.

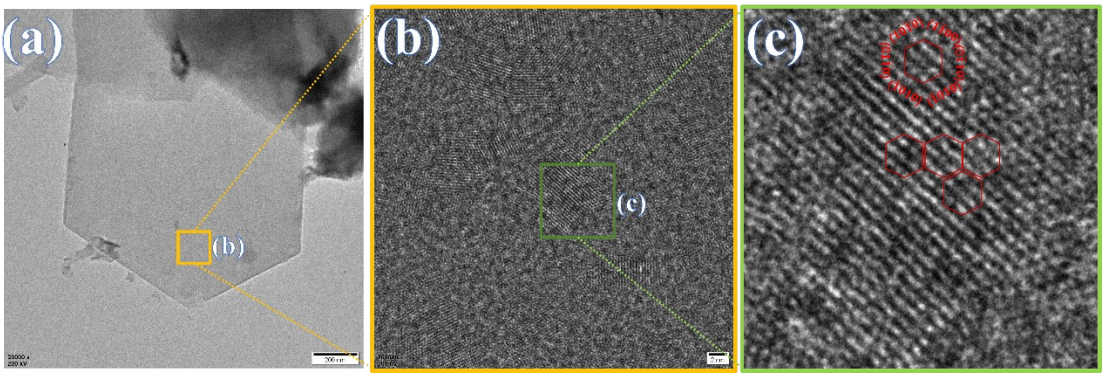

Fig. S21. (a-c) Gradually enlarged TEM image $Mo_{4/3}B_{2-x}T_z$ prepared by us.

In situ Raman analysis of NF and TBAOH/NF

To prove that more NiOOH active substances are produced on the surface of NF after TBAOH treatment, In-situ Raman test was performed on NF and TBAOH/NF. **In Supplementary Fig. S22,** at 1.25 V of applied voltage, two Raman bands appear at 458 cm^{-1} and 527 cm^{-1}, which are well indexed to the Ni-OH and Ni-O vibrational bands of Ni(OH), respectively(*Adv. Funct. Mater.* 31 (2021), e2101820). At 1.45 V of applied voltage, the two vibrational bands of Ni(OH) were red-shifted to

473 cm^{-1} and 554 cm^{-1}, which are well pointing in δ(Ni-O) vibrational band and ν(Ni-O) stretching vibrational band of NiOOH, respectively (*Adv. Mater*. 34 (2022), e2108619). At 1.65V of applied voltage, the position of the Raman band remains unchanged and the Ni-O vibration peak of NiOOH at 473 and 554 cm^{-1} gradually strengthen. By comparing the in-situ Raman graphs of NF and TBAOH/NF, we found that TBAOH/NF has a higher response value in terms of Ni-O vibration peak of NiOOH at 473 and 554 cm^{-1}, which proves that TBAOH/NF surface does produce more NiOOH. To verify that TBAOH has more positive charge than NF, we prepare new samples of NF and TBAOH/NF for direct EIS testing. **In Supplementary Figure 23,** at high frequency, it is found that Log(|Z|) of TBAOH/NF has a greater decline than NF as the frequency decreases. This is because charge transfer plays a leading role in the high frequency region rather than material transfer and more charge leads to a larger space for impedance decline. Therefore, this implies that the surface of TBAOH/NF has more positive charges.

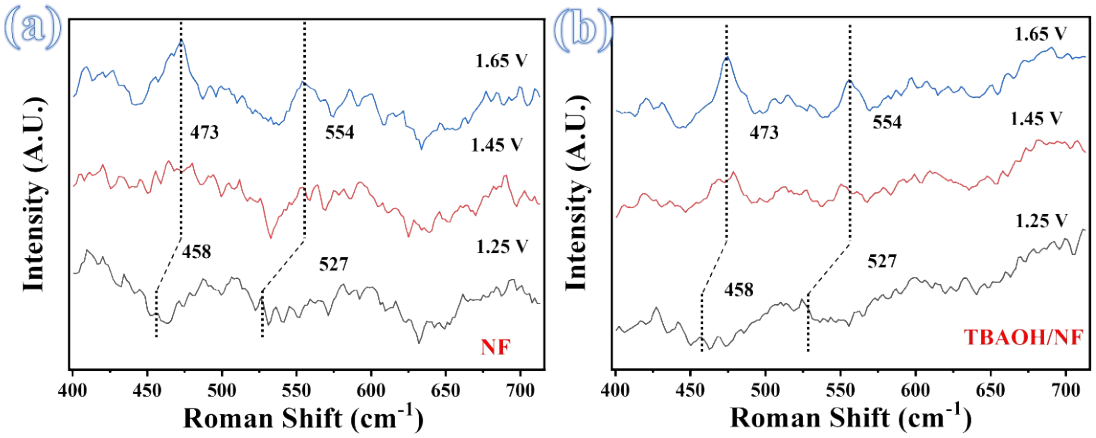

Fig. S22. In-situ Roman spectra of NF and TBAOH/NF.

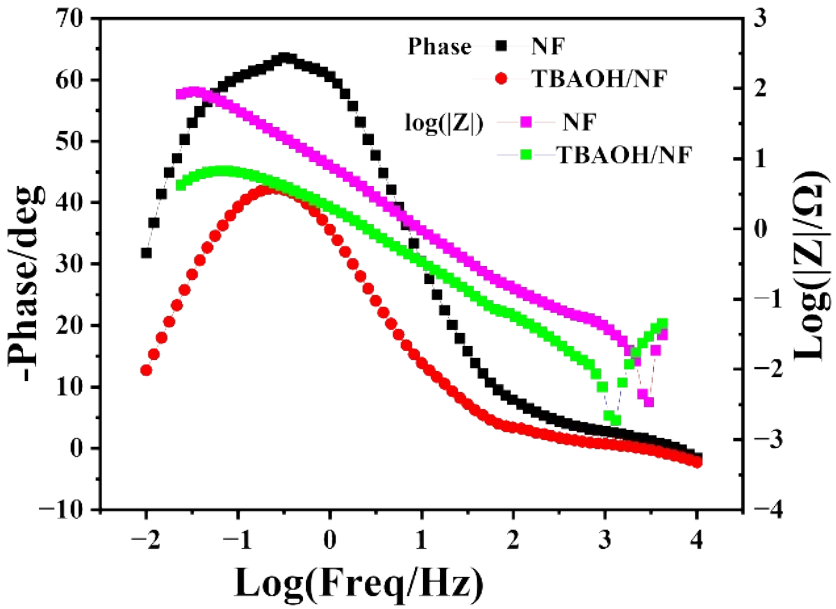

Fig. S23. Bode plot of NF and TBAOH/NF.

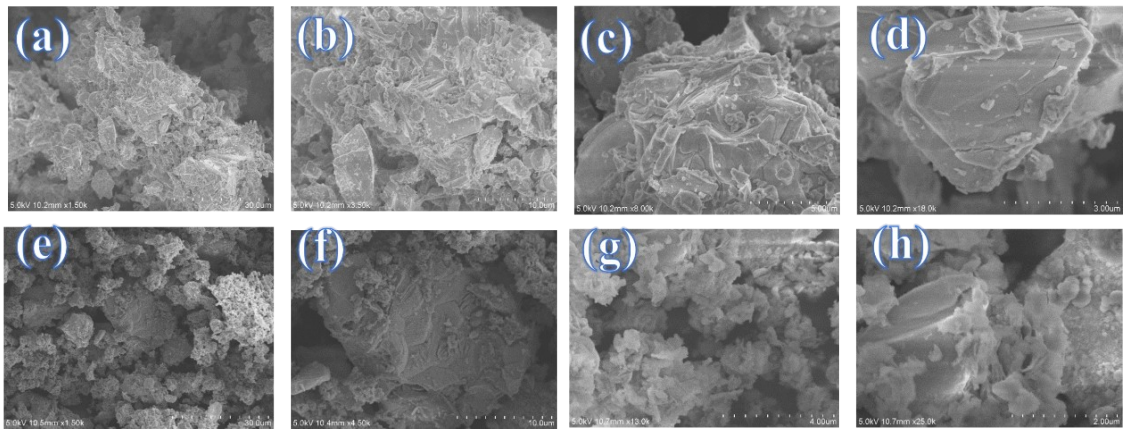

Fig. S24. (a-d) SEM images $(Mo_{2/3}Y_{1/3})_2AlB_2$ before etched. (e-h) SEM images $(Mo_{2/3}Y_{1/3})_2AlB_2$ after etched.

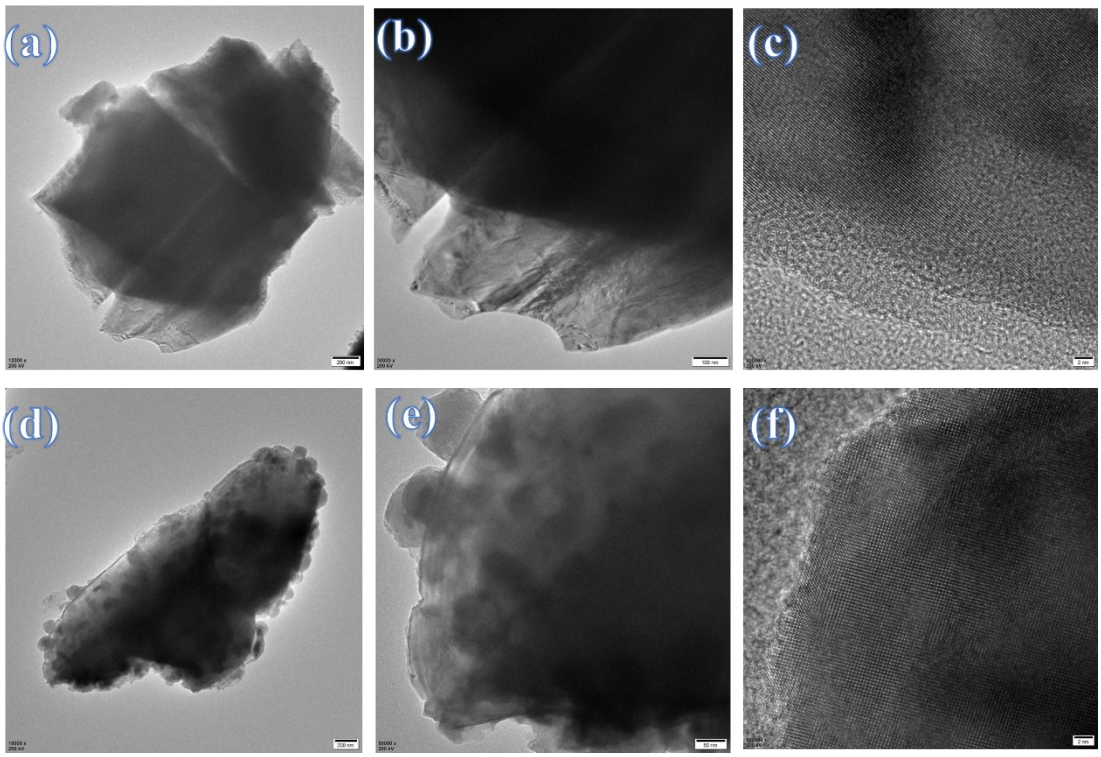

Fig. S25. (a-c) TEM images $(Mo_{2/3}Y_{1/3})_2AlB_2$ before etched. (d-f) TEM images $(Mo_{2/3}Y_{1/3})_2AlB_2$ after etched.

References

[1] Zhao P, Nie H, Zhou Z, et al. NiFe-LDH Grown on Three-Dimensional Cu_3P Nano-Array for Highly Efficient Water Oxidation [J]. ChemistrySelect, 2018, 3(28): 8064-8069.

[2] Wang M H, Lou Z X, Wu X, et al. Operando High-Valence Cr-Modified NiFe Hydroxides for Water Oxidation [J]. Small, 2022, 18(19): 2200303.

[3] Gao K, Xu M, Zhang C, et al. Rapid fabrication of $NiFe(OH)_x/Fe_{0.2}Co$-Se complexes for oxygen evolution reaction electrocatalysis[J]. Journal of Industrial and Engineering Chemistry, 2023, 124: 263-269.

[4] Li Z, Wang X, Ren J, et al. NiFe LDH/$Ti_3C_2T_x$/nickel foam as a binder-free electrode with enhanced oxygen evolution reaction performance[J]. International Journal of Hydrogen Energy, 2022, 47(6): 3886-3892.

[5] Wang X, Wang J, Liao J, et al. Surface engineering of superhydrophilic Ni_2P@NiFe LDH heterostructure toward efficient water splitting electrocatalysis[J]. Applied Surface Science, 2022, 602: 154287.

[6] Guo D, Yu H, Chi J, et al. Cu_2S@NiFe layered double hydroxides nanosheets hollow nanorod arrays self-supported oxygen evolution reaction electrode for efficient anion exchange membrane water electrolyzer[J]. International Journal of Hydrogen Energy, 2023, 48(47): 17743-17757.

[7] Han C, Ji Z, Zhu Y, et al. Construction of Ni_3S_2-Ni_xP_y/NF@NiFe LDH with heterogeneous interface to accelerate catalytic kinetics of overall water splitting[J].

Materials Research Letters, 2022, 10(11): 762-770.
[8] Zhang X, Xue Y, Yan Q, et al. Hydrangea-like sulfide NiFe layered double hydroxides grown on an undulate nickel framework as bifunctional electrocatalysts for overall water splitting[J]. Materials Today Energy, 2021, 21: 100741.
[9] Du F, Ling X, Wang Z, et al. Strained heterointerfaces in sandwich–like NiFe layered double hydroxides/$Co_{1-x}S$ for highly efficient and superior long–term durable oxygen evolution reaction[J]. Journal of Catalysis, 2020, 389: 132-139.
[10] Gan Y, Ye Y, Dai X, et al. Self-sacrificial reconstruction of MoO_4^{2-} intercalated NiFe LDH/Co_2P heterostructures enabling interfacial synergies and oxygen vacancies for triggering oxygen evolution reaction[J]. Journal of Colloid and Interface Science, 2023, 629: 896-907.
[11] Wang S, Ge X, Lv C, et al. Oxygen vacancy-rich amorphous porous NiFe(OH)x derived from Ni(OH)x/Prussian blue as highly efficient oxygen evolution electrocatalysts[J]. Nanoscale, 2020, 12(17): 9557-9568.
[12] Mao L, Hao X, Zhang Y, et al. Hierarchical Cu Nanoarray/NiFe Hydroxide Nanostructures for Efficient Electrochemical Water Oxidation[J]. ACS Applied Nano Materials, 2023, 6(11): 9857-9864.